



Cite this: *Nanoscale Horiz.*, 2025, 10, 1398

Received 10th April 2025,
Accepted 15th May 2025

DOI: 10.1039/d5nh00224a

rsc.li/nanoscale-horizons

TMB (TM = Cr, Fe) monolayers: a new type of room temperature antiferromagnetic topological nodal line semimetal†

Chenqian Yan, Yuqing Mao, Jie Li, Zijin Wang, Ailei He,* Yuanyuan Duan and Xiuyun Zhang *

Two-dimensional materials that combine magnetism and topology offer unique advantages in the fields of spintronics and quantum computing. However, the design of two-dimensional (2D) materials simultaneously integrating both properties remains a significant challenge. Through systematic first-principles calculations, we predict two highly stable two-dimensional transition metal borides (TMBs). Our results reveal that both structures are antiferromagnetic (AFM) Dirac nodal line semimetals (NLSMs) with multiple band crossings near the Fermi level. Under biaxial strain, FeB can be transformed into a ferromagnetic state under 2% tensile strain, which is further verified

College of Physics Science and Technology, Yangzhou University, Yangzhou 225002, China. E-mail: heailei@yzu.edu.cn, xyzhang@yzu.edu.cn

† Electronic supplementary information (ESI) available: Band structures of FeB and CrB monolayers with different U values added; Poisson's ratios of the FeB (a) and CrB (b) monolayers; the band structure of (a) FeB and (b) CrB monolayers with SOC applied along the z-direction; band structure of FeB (a) and CrB (b) under DFT calculations and the tight-binding model; the band structure of FeB and CrB monolayers in the range of $\epsilon = -4\%$ to 4% . See DOI: <https://doi.org/10.1039/d5nh00224a>



Xiuyun Zhang

topological properties and their applications in spintronic devices and electrochemical catalytic performance.

Dr Xiuyun Zhang is a Professor in College of Physics Science and Technology, Yangzhou University. She got her PhD degree in physics from Southeast University in 2010, and carried out her postdoctoral research in Hong Kong Polytechnic University from 2011 to 2013. Currently, her research interest is the fundamental properties and potential applications of low dimensional systems, including the growth mechanism, the electronic and magnetic properties, the

New concepts

Two-dimensional antiferromagnetic nodal-line semimetals represent an emerging frontier in condensed matter physics and materials science. When two electronic bands intersect in a solid, they form one-dimensional nodal lines within the Brillouin zone. In single-particle systems, these topological features invariably form closed loops, commonly termed nodal loops in the literature. Current research on nodal lines has expanded along two novel dimensions: (i) nodal lines in 2D materials. (ii) nodal lines in magnetic systems. However, 2D materials exhibit exceptional mechanical properties and broad tunability, while antiferromagnetism offers distinct advantages including zero net magnetic moment, negligible stray fields, and ultrafast magnetic response. Through first-principles calculations, we have successfully predicted a new class of boron-based 2D antiferromagnetic materials. These structures ingeniously integrate antiferromagnetic ordering with nodal-line semimetallic characteristics in two-dimensional systems, demonstrating remarkable potential for applications in spintronics and quantum computing technologies.

to possess Weyl nodal loops (Weyl NLs). This discovery provides novel insights for the regulation of magnetic topological materials and holds promising potential for applications in low-power-consumption spintronic devices.

Introduction

In condensed matter physics and materials science, the interaction between magnetic and topological properties^{1–4} has stimulated strong research interest in spintronics. In particular, the emergence of two-dimensional (2D) materials provides an ideal platform for the design and control of nanoscale spintronic devices.^{5–7} Among these materials, magnetic topological semimetals (MTSS)^{8–10} have the feature of a gapless bulk-band structure where the conduction and valence bands cross each other in the Brillouin zone (BZ), and have attracted tremendous research interest. The band crossings of the MTSS are protected by the combination of exact crystal symmetry and topology.

According to the dimensionality and nature of their band crossings, 2D MTSs can be classified into two categories: (i) nodal point semimetals, whose energies are dispersed linearly along all momentum directions around the point nodes. They can be classified into Dirac semimetals (DSMs) with quadruple nodal degeneracy,¹¹ and Weyl semimetals (WSMs) with double nodal degeneracy,^{12,13} the latter of which requires either the inversion symmetry or the time reversal symmetry to be broken. (ii) Nodal-line semimetals (NLSMs), characterized with the nontrivial nodal line state in the Brillouin zone (BZ), formed by the one-dimensional band crossings in the low-energy band structures. They can be classified into Dirac NLSMs and Weyl NLSMs.^{14–17}

The rapid development of 2D ferromagnetic (FM) materials can be traced back to the successful fabrication of 2D van der Waals (vdW) crystals of Cr₂Ge₂Te₆¹⁸ and CrI₃.¹⁹ Accordingly, some topological NLSM candidates in FM 2D materials were found, such as MnN,²⁰ GdCl,²¹ Cu₂Si²² and h-InC,²³ GdAg₂,²⁴ and Fe₃GeTe₂,²⁵ metal organic frameworks,¹⁴ *etc.* Compared with FM candidates, the zero net magnetization of antiferromagnetic (AFM) materials makes them less susceptible to external magnetic fields.²⁶ Moreover, the interplay between AFM and band topology has emerged as a rich frontier in condensed matter physics, giving rise to novel phenomena such as spin-split bands and magnetic Weyl fermions.²⁷ However, most discovered AFM-NLSMs are 3D materials,^{28–30} and few are found for 2D candidates, including TM₂B₃, germanene/Mn₂S₂,³¹ MoB₃ monolayer,³² CrAs₂,¹⁵ and MnC₄.³³ Considering the great success in the field of graphene, it is expected that searching for 2D AFM-NLSMs will most likely lead to the discovery of numerous noteworthy physical phenomena and novel topological states.

In our study, we predicted two highly stable 2D transition metal borides, TMB (TM = Cr, Fe), through first-principles calculations. Both TMBs are found to favor AFM ground states with Néel temperatures (T_N s) of 240 K and 712 K, respectively. Moreover, both CrB and FeB monolayers exhibit AFM NLSM features accompanied by multiple Dirac points around the Fermi level. By applying biaxial strains, we found that the FeB monolayer can be transitioned into a FM Weyl NLSM.

Computational methods

All first-principles calculations were carried out based on density functional theory (DFT) implemented in the Vienna *ab initio* simulation package (VASP).^{34,35} The exchange–correlation functional was treated using the Perdew–Burke–Ernzerhof (PBE)³⁶ method, which is based on the generalized gradient approximation (GGA);³⁷ meanwhile the interaction between electrons and ions was described by the projector-augmented wave (PAW) method.³⁸ The energy cutoff was set at 400 eV. The convergences for force and energy were -0.001 eV Å⁻¹ and 10^{-6} eV, respectively. Given the strongly correlated interactions of 3d TM elements, the GGA+*U* method (U_{eff}) was employed. To verify the impact of U_{eff} on the magnetic ground states of both TMB monolayers, we examined the magnetic ground state by varying U_{eff} within the range of 2–5 eV. As a result, no appreciable

variations were detected, as shown in Fig. S1 (ESI[†]). Based on the analysis, the Hubbard corrections of $U_{\text{eff}} = 4$ eV were chosen in this study to analyse the electronic structure, which has been adopted in previous literature.^{39,40} In geometry optimization and electronic property analysis, the Brillouin zone was sampled using a $15 \times 15 \times 1$ and $25 \times 25 \times 1$ centered Monkhorst–Pack grid. The vacuum layer with a thickness of 15 Å is applied to avoid the interaction between periodic images.

The PHONOPY program, based on density functional perturbation theory (DFPT)⁴¹ was utilized to calculate the phonon dispersion spectra of the $4 \times 4 \times 1$ supercells of FeB and CrB monolayers. *Ab initio* molecular dynamics (AIMD) simulations were employed using $3 \times 3 \times 1$ supercells at the temperature of 300 K for 6 ps to evaluate the thermal stability. Second-order perturbation theory was performed to calculate the magnetic anisotropy energy (MAE).⁴² In addition, the T_N s of both monolayers were calculated, with a lattice of $100 \times 50 \times 1$ adopted in the Monte Carlo (MC) simulations by using the EspinS package.⁴³

Results and discussion

Top and side views of the TMB (TM = Cr, Fe) monolayer are shown in Fig. 1(a), in which the TM ions and B ions form a tetragonal sublattice, and the space group of both monolayers is *P4/mmm*. The lattice constants of the CrB and FeB monolayers are $a = b = 2.73$ Å and 2.85 Å, respectively, with the Fe–B and Cr–B bond lengths of around 1.93 Å and 2.02 Å, respectively (see Table 1). To verify the experimental feasibility of these materials, we calculated the formation energy (E_f) by using eqn (1),

$$E_f = [E(\text{TMB}) - \mu(\text{TM}) - \mu(\text{B})]/2, \quad (1)$$

we found that they were all negative, indicating that the FeB and CrB monolayers are more stable than the separated pure components. The thermal and dynamic stability of this TMB monolayer is evaluated by following two routes. First, the phonon dispersion spectra of both TMB monolayers were calculated, and as shown in Fig. 1(b), there is no imaginary frequency throughout the Brillouin zone (BZ), indicating that both systems exhibit dynamic stability. Secondly, the AIMD simulations at 300 K are shown in Fig. 1(c) and (f), where the insets are the structures of the CrB and FeB monolayers at the end of 6 ps. It is clear that the energy fluctuates slightly and their frameworks are not destroyed, suggesting their thermal stabilities at room temperature. Fig. 1(d) shows the electron localization function (ELF) of the FeB monolayer. It is found that the ELF values at the positions of the Fe atoms are relatively low, whereas the ELF values between the Fe atom and B atom are close to 0.5. Therefore, we can conclude that there are stable covalent bonds between the atoms in this structure. To determine their mechanical stability, we calculated the elastic constants of C_{11} , C_{12} , C_{22} , and C_{66} for both monolayers (see Table S1 in the ESI[†]), which are found to satisfy the Born mechanical stability criteria ($C_{11} > 0$, $C_{11} \cdot C_{22} > C_{12}^2$, and $C_{66} > 0$), implying that they are mechanically stable. Besides, we calculated their Young's modulus (Y) and

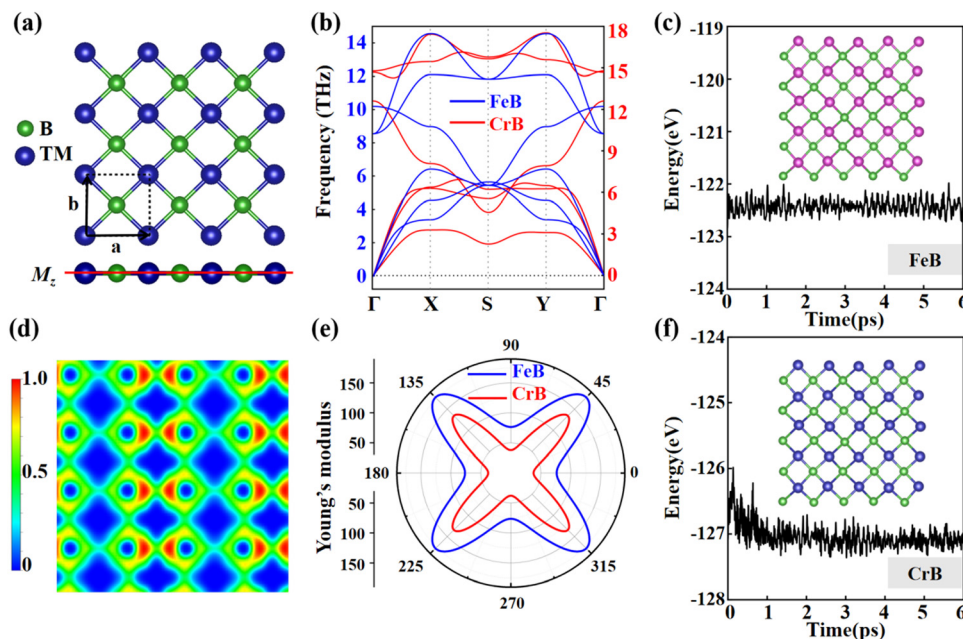


Fig. 1 (a) Top and side views of the geometry for monolayer TMB (TM = Fe, Cr). The unit cell is denoted by the dotted line. (b) The phonon spectra of the FeB (blue) and CrB (red) monolayers. The variation of total energies of FeB (c) and CrB (f) in the AIMD simulated structure at 300 K. Insets are the frameworks of both monolayers at the end of 6 ps. (d) The calculated electron localization function (ELF) of the FeB monolayer for the (001) plane. (e) Young's modulus of the FeB (blue) and CrB (red) monolayers.

Poisson's ratios (ν), respectively, based on eqn (2) and (3),

$$Y(\theta) = \frac{C_{11}C_{22} - C_{12}^2}{C_{11}\sin^4\theta + A\sin^2\theta\cos^2\theta + C_{22}\cos^4\theta}, \quad (2)$$

$$\nu(\theta) = \frac{C_{12}\sin^4\theta - B\sin^2\theta\cos^2\theta + C_{12}\cos^4\theta}{C_{11}\sin^4\theta + A\sin^2\theta\cos^2\theta + C_{22}\cos^4\theta}, \quad (3)$$

where $A = \frac{C_{11}C_{22} - C_{12}^2}{C_{66}} - 2C_{12}$ and $B = C_{11} + C_{22} - \frac{C_{11}C_{22} - C_{12}^2}{C_{66}}$. As shown in Fig. 1(e) and Fig. S2 in the ESI,[†] both monolayers exhibit anisotropic Young's modulus and Poisson's ratios.

In order to determine the magnetic ground states of the FeB and CrB monolayers, three different magnetic configurations are considered in a 2×2 supercell, including the FM state and two types of AFM (AFM1, AFM2) states, as shown in Fig. 2(a). Our calculations show that both monolayers favor the AFM1 states with the local magnetic moments per Cr/Fe atom of $2.16/3.02\mu_B$. In both monolayers, the energy differences between the AFM ground states and FM states are about 0.22 eV and 1.03 eV per unit cell for the FeB and CrB monolayer, respectively. To

determine the magnetic stability, we calculated the angular dependence of the magnetic anisotropic energy (MAE) of the FeB (Fig. 2(b)) and CrB (Fig. 2(c)) monolayers, respectively. For both systems, the total energy of the out-of-plane (z) direction is the lowest with considerable MAE values of 1.15 meV and 9.0 meV for the TM atom, respectively, indicating that their easy

Table 1 Lattice constants (a and b , Å), TM–B bond length ($d_{\text{TM-B}}$, Å), TM–TM–TM bond angle (α_1 , degree), TM–B–TM bond angle (α_2 , degree), formation energy (E_f , eV), energy difference between FM and AFM-1 states ($\Delta E = E_{\text{FM}} - E_{\text{AFM-1}}$, eV), and ground states (GS) of the TMB (TM = Fe, Cr) monolayers

System	a (Å)	b (Å)	$d_{\text{TM-B}}$ (Å)	α_1 (°)	α_2 (°)	E_f (eV)	ΔE (eV)	GS
FeB	2.73	2.73	1.93	90.00	90.0	-6.87	0.22	AFM metal
CrB	2.85	2.85	2.02	90.00	90.0	-7.08	1.03	AFM metal

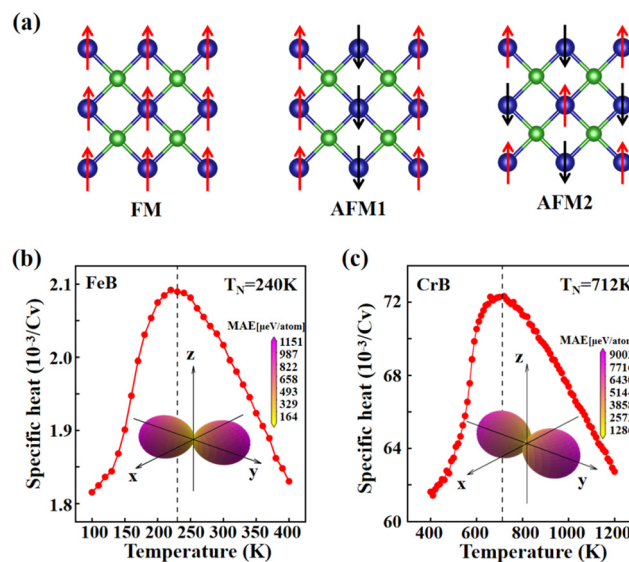


Fig. 2 (a) Spin configurations of the FM state and two AFM (AFM1, and AFM2) states. Specific heat as functions of temperature and MAE of FeB (b) and CrB (c) monolayers. Insets are the angular dependence of the magnetic anisotropic energy (MAE) of FeB (b) and CrB (c) monolayers, respectively.

magnetization axes are in the z direction. Next, the T_{NS} of both systems were extended by performing classical MC simulations in the Heisenberg spin Hamiltonian in eqn (4):

$$H = - \sum_{ij} J_{ij} \vec{S}_i \cdot \vec{S}_j - \sum_i A (S_i^z)^2, \quad (4)$$

where \vec{S}_i represents the magnetic moment of the atom at site i , and J_1 , J_2 , and J_3 denote the nearest-neighbor (NN), second-nearest-neighbor (NNN), and third-nearest-neighbor (3NN) exchange coupling parameters, respectively. As shown in the specific heat plots of Fig. 2(b) and (c), the T_{NS} for FeB and CrB are around 240 K and 712 K, respectively, close to or over room temperature, which proves their potential for applications in spintronic devices.

The element-resolved band structures of FeB and CrB monolayers are shown in Fig. 3(a)–(d), respectively, in which the Fe and Cr elements contribute more significantly to the band structures near the Fermi level. In particular, it is found that the valence and conduction bands meet in the vicinity of the Fermi level, resulting in three intersection points, P1, P2, and P3, which are marked by green circles in Fig. 3(b) and (e). Moreover, these band crossing points exhibit fourfold degeneracy because of their overlapping spin-up and spin-down channels induced by the presence of PT symmetry [the combined symmetry of spatial-inversion (P) and time-reversal (T)]. Further analysis shows that the NLs along the k_x direction for FeB and CrB monolayers are formed in the entire BZ by three

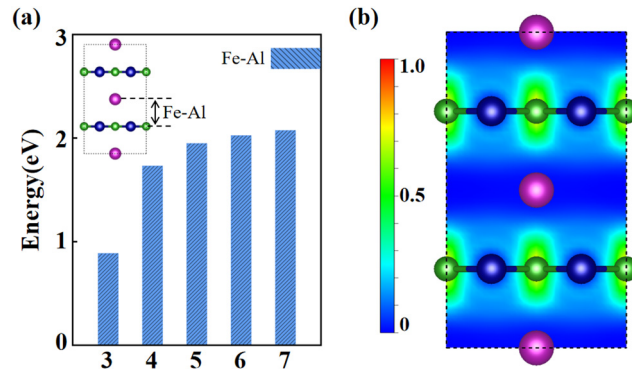


Fig. 4 (a) Comparison of the strength of Fe–Al bonds under different band lengths. (b) The ELF contour plots of the FeB monolayer.

Dirac points (P1, P2, P3), which belong to the open NL as shown in Fig. 3(c) and (f). By considering spin-orbital coupling (SOC)⁴⁴ with the magnetization direction along the z axis, all the nodal points are gapped with small band gaps, as shown in Fig. S3(a) and (b) in the ESI,[†] due to the breaking of a specular mirror-reflection symmetry (σ_h). Moreover, due to the presence of σ_h symmetry in the FeB and CrB monolayers, all momentum points are hosted in the small group of C_s in the 2D BZ. The opposite two linear cross bands belong to different irreducible representations (IRs) of Γ_1 and Γ_2 with mirror eigenvalues of 1 and -1 . An inspection of IR in the two bands reveals that the ordering of the CB and VB is inverted, forming a continuous

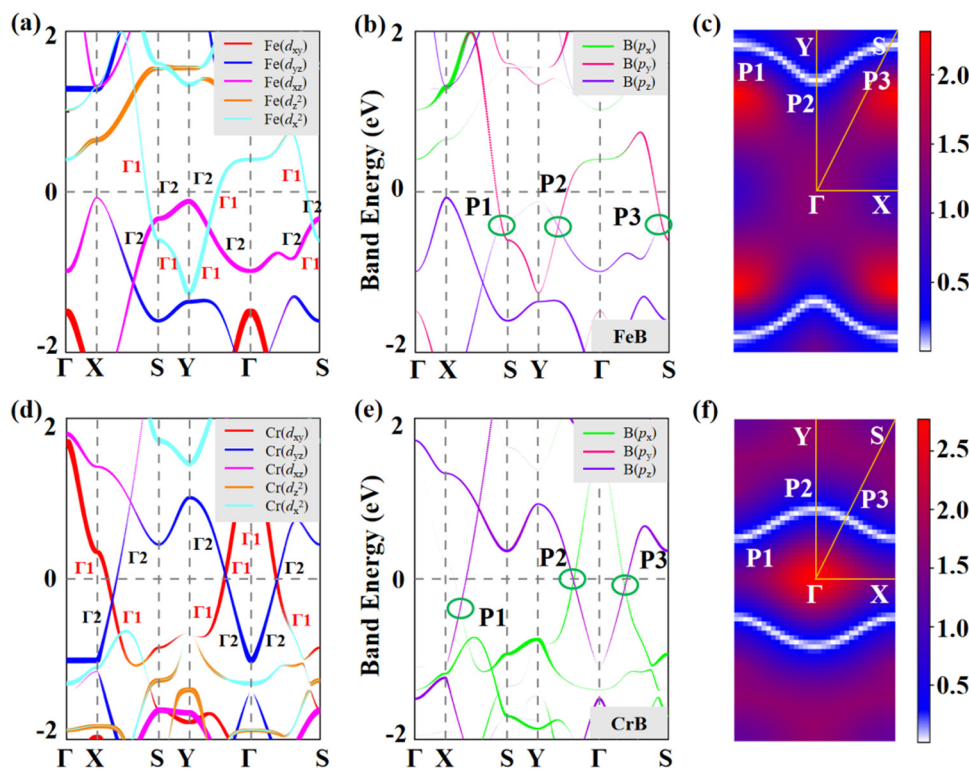


Fig. 3 The orbital-projected band structures of (a) Fe and (b) B atoms in the FeB monolayer, and (d) Cr and (e) B atoms in the CrB monolayer. The “T1” and “T2” represent the eigenvalue of mirror M_z with 1 and -1 , respectively. The diagram of the gap size at the Fermi level in BZ of (c) FeB and (f) CrB monolayers.

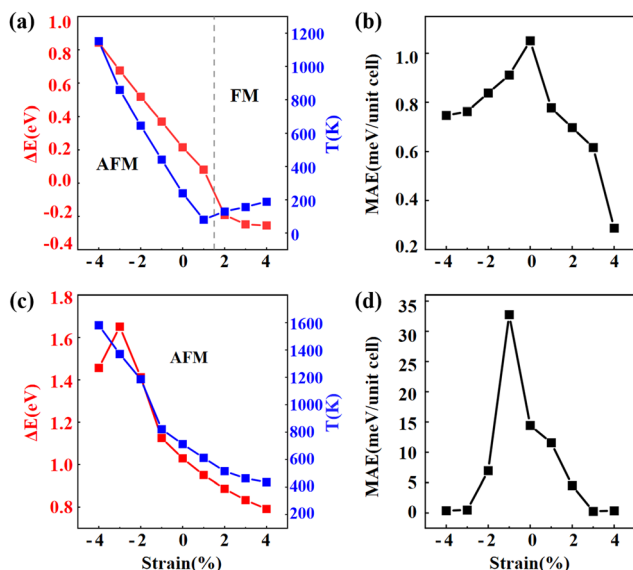


Fig. 5 Energy differences (ΔE , red line) and the T_N (blue line) as a function of strain for FeB (a) and CrB (c) monolayers. The MAE as a function of strain for FeB (b) and CrB (d) monolayers.

nodal-ring around the Γ point. This is responsible for the existence of this topological nontrivial state. Seen from Fig. 3, we can observe that the bands near the Fermi level are primarily composed of the d orbitals of metal atoms and the p orbitals of non-metal atoms. Therefore, we constructed a tight-binding (TB) model based on the p orbitals of non-metal atoms and the d orbitals of metal atoms by using the maximally localized

Wannier functions, and it can be observed that its band structure nearly coincides with the DFT-calculated bands at the Fermi level, as shown in Fig. S4 in the ESI.†

In order to experimentally validate viable synthetic routes for FeB and CrB monolayers, we used the most commonly used method, *i.e.* selective etching of aluminium metal layers from the MAB bulk phase.^{45,46} By setting the Fe–Al bond lengths from 3 to 7 Å and comparing their energies with those at a bond length of 2.5 Å, as shown in Fig. 4(a), our findings demonstrate that the energy difference increases with Fe–Al bond length in the FeAlB material, where longer Fe–Al distances correspond to higher system energies. This energetically favors Al layer exfoliation, thereby facilitating the synthesis of FeB monolayer materials. Moreover, the ELF counter plot of bulk FeAlB is shown in Fig. 4(b), and it is evident that the ELF value for the Fe–Al bond is close to 0, while the ELF value for the Fe–B bond is close to 0.5, indicating that the covalent bonding strength of the Fe–B bond is significantly stronger than that of the Fe–Al bond.

Finally, we explored the effect of biaxial strains (ε) on the electronic and magnetic properties of these 2D materials, where $\varepsilon = (a - a_0)/a_0$, and a and a_0 are the lattice constants with and without strain. The red line in Fig. 5(a) and (c) represents the energy differences between the FM and the lowest-energy AFM states of the FeB and CrB monolayer. It is clear that the energy differences are in the range of 0–1 eV and 0.8–1.8 eV for FeB and CrB, respectively. In the range of $\varepsilon = -4\%$ to 1%, the FeB monolayer retains its AFM metallic properties; when subjected to a tensile strain of 2%, it is changed to be a

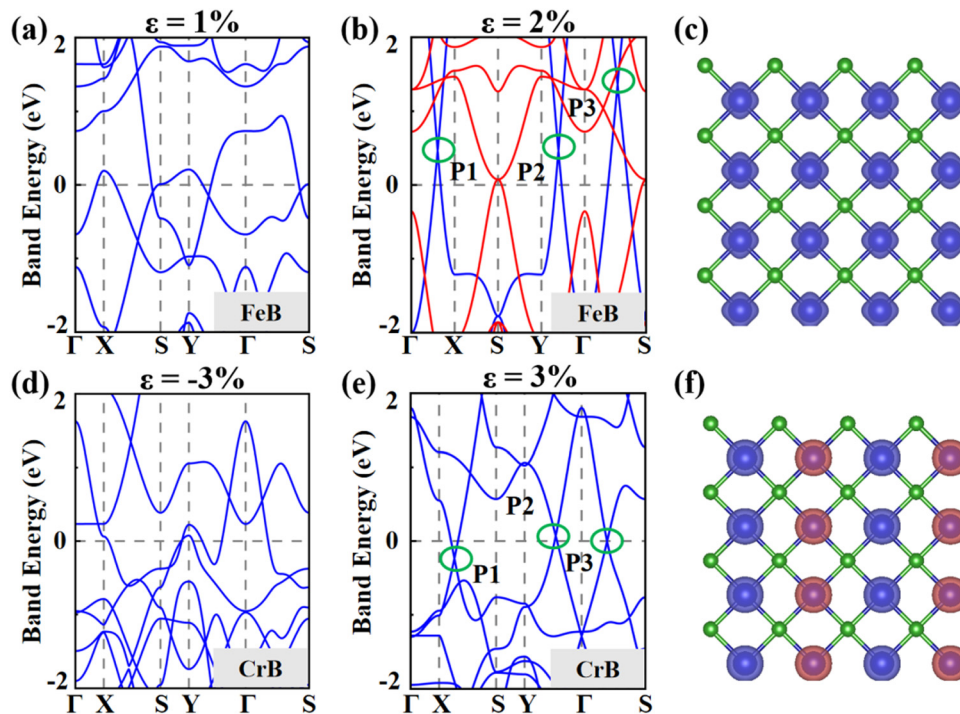


Fig. 6 Band structures of the FeB monolayer under tensile strains of 1% (a), and 2% (b). (c) Spin density map of FeB under 2% tensile strain. Band structures of CrB monolayer under $\varepsilon = -3\%$ (d), and 3% (e). (f) Spin density map of CrB under 3% tensile strain.

FM metal. Differently, the CrB monolayer consistently maintains its AFM metallic characteristics in the range of $\varepsilon = -4\%$ to 4% . As shown by the blue line in Fig. 5(a) and (c), the T_{NS} of the AFM FeB and CrB monolayers exhibit a monotonic decreasing trend within the strain ranges of $\varepsilon = 4\%$ to 1% and $\varepsilon = -4\%$ to 4% , respectively. In contrast, for the strains ranging from 2% to 4% , the Curie temperature (T_{C}) of the FM FeB monolayer shows an increasing trend. Importantly, in most cases, the T_{NS} remain above room temperature, enhancing their spintronic device applicability. Moreover, the strain-dependent MAEs for both monolayers are analyzed and presented in Fig. 5(b) and (d). The MAEs of both monolayers exhibit a decreasing trend under tensile strain. Notably, their responses to compressive strain differ significantly, in which the FeB material shows a continuous MAE enhancement, while for CrB, it displays an initial increase followed by a decrease. Also, the easy axis for all systems remained to be along the z -direction throughout the strain variations.

The band structures of FeB and CrB monolayers under different biaxial strains (ε) are shown in Fig. 6(a), (b), (d) and (e) and Fig. S5 and S6 in the ESI.† For the FeB monolayer, it retains AFM NLSM properties under 1% tensile strain as well as compressive strain, whereas under 2% or larger tensile strain, the spin up and spin down channels of the FeB monolayer are split and the system is changed to the FM state (see Fig. 6(b) and Fig. S5(b)–(d) in the ESI.†). As shown in Fig. 6(b) and S7(a) in the ESI,† there are three band crossing points with double degeneracy that appear near the Γ point (marked by green circles above the Fermi level) of FeB, with additional experimental evidence confirming the formation of a closed nodal loop within the BZ, indicating that it is transitioned to be FM Weyl NLSM. As for the CrB monolayer, it retains AFM NLSM properties under tensile and compressive strains, as shown in Fig. S6 and S7(b) in the ESI.†

In conclusion, through first-principles calculations, we have successfully predicted two stable 2D TMB monolayers, FeB and CrB monolayer. Our results show that both monolayers exhibit thermal, dynamic, and mechanical stabilities. Both TMB monolayers have AFM states with high T_{NS} and large MAEs. Moreover, FeB and CrB monolayers are robust AFM NLSMs with several Dirac cones near the Fermi level. Besides, the CrB monolayer maintains the AFM NLSM property in the range of $\varepsilon = -4\%$ to 4% , while the AFM NLSM property of the FeB monolayer is subjected to a biaxial tensile strain of 1% , and then it transitions to a FM NLSM under larger tensile strains. Our results propose a potential way to design 2D TM borides with promising magnetic and topological properties.

Data availability

The data supporting this article have been included as part of the ESI.†

Conflicts of interest

There are no conflicts to declare.

Acknowledgements

This work is supported by the National Natural Science Foundation of China (Grant No. 12004098, 12104130) and the Yangzhou University Student Science and Innovation Project (XCX20240283). We acknowledge the computational resources at Yangzhou University.

References

- 1 C. Fang, H. M. Weng, X. Dai and Z. Fang, *Chin. Phys. B*, 2016, **25**, 117106.
- 2 F. D. M. Haldane, *Phys. Rev. Lett.*, 1998, **61**, 2015.
- 3 Y. Deng, Y. Yu, M. Z. Shi, Z. Guo, Z. Xu, J. Wang, X. H. Chen and Y. Zhang, *Science*, 2020, **367**, 895–900.
- 4 T. Li, S. Jiang, B. Shen, Y. Zhang, L. Li, Z. Tao, T. Devakul, K. Watanabe, T. Taniguchi, L. Fu, J. Shan and K. F. Mak, *Nature*, 2021, **600**, 64–646.
- 5 K. S. Novoselov, A. K. Geim, S. V. Morozov, D. Jiang, Y. Zhang, S. V. Dubonos, I. V. Grigorieva and A. A. Firsov, *Science*, 2004, **306**, 666–669.
- 6 J.-C. Lei, X. Zhang and Z. Zhou, *Front. Phys.*, 2015, **10**, 276–286.
- 7 S. Z. Butler, S. M. Hollen, L. Cao, Y. Cui, J. A. Gupta, H. R. Gutiérrez, T. F. Heinz, S. S. Hong, J. Huang, A. F. Ismach, E. Johnston-Halperin, M. Kuno, V. V. Plashnitsa, R. D. Robinson, R. S. Ruoff, S. Salahuddin, J. Shan, L. Shi, M. G. Spencer, M. Terrones, W. Windl and J. E. Goldberger, *ACS Nano*, 2013, **7**, 2898–2926.
- 8 W. Meng, X. Zhang, T. He, L. Jin, X. Dai, Y. Liu and G. Liu, *J. Adv. Res.*, 2020, **24**, 523–528.
- 9 L. Jin, X. Zhang, T. He, W. Meng, X. Dai and G. Liu, *Appl. Surf. Sci.*, 2020, **520**, 146376.
- 10 C. Zhang, Z. Yuan, Q. Jiang, B. Tong, C. Zhang, X. C. Xie and S. Jia, *Phys. Rev. B*, 2017, **95**, 085202.
- 11 Z. Wang, Y. Sun, X. Chen, C. Franchini, G. Xu, H. Weng, X. Dai and Z. Fang, *Phys. Rev. B*, 2012, **85**, 195320.
- 12 S. Murakami, *New J. Phys.*, 2007, **9**, 356.
- 13 X. Wan, A. M. Turner, A. Vishwanath and S. Y. Savrasov, *Phys. Rev. B*, 2011, **83**, 205101.
- 14 Y. Wang, J. Jiang and W. Mi, *J. Phys. Chem. C*, 2022, **126**, 9998–10006.
- 15 B. Wang, H. Gao, Q. Lu, W. Xie, Y. Ge, Y.-H. Zhao, K. Zhang and Y. Liu, *Phys. Rev. B*, 2018, **98**, 115164.
- 16 C. W. Niu, J.-P. Hanke, P. M. Buhl, H. B. Zhang, L. Plucinski, D. Wortmann, S. Blügel, G. Bihlmayer and Y. Mokrousov, *Nat. Commun.*, 2019, **10**, 3179.
- 17 W. L. Sun, B. Y. Li, X. R. Zou, R. H. Li, B. B. Huang, Y. Dai and C. W. Niu, *Adv. Sci.*, 2023, **10**, 2301474.
- 18 C. Gong, L. Li, Z. Li, H. Ji, A. Stern, Y. Xia, T. Cao, W. Bao, C. Wang, Y. Wang, Z. Q. Qiu, R. J. Cava, S. G. Louie, J. Xia and X. Zhang, *Nature*, 2017, **546**, 265–269.
- 19 B. Huang, G. Clark, E. Navarro-Moratalla, D. R. Klein, R. Cheng, K. L. Seyler, D. Zhong, E. Schmidgall, M. A. McGuire, D. H. Cobden, W. Yao, D. Xiao, P. Jarillo-Herrero and X. Xu, *Nature*, 2017, **546**, 270–273.

- 20 S. S. Wang, Z. M. Yu, Y. Liu, Y. Jiao, S. Guan, X. L. Sheng and S. A. Yang, *Phys. Rev. Mater.*, 2019, **3**, 084201.
- 21 Y. Wang, X. Zhang, Z. Gao, T. Cao, J. Shi and X. Fan, *J. Phys. Chem. C*, 2023, **127**, 4375–4832.
- 22 J. Xu, C. Liu, X. Y. Guo, J. K. Zhang, K. Liu, H. J. Qian, K. Q. Nie, Z. Y. Wang and J. Wang, *Surf. Sci.*, 2025, **752**, 122632.
- 23 S. Jeon, Y.-T. Oh and Y. Kim, *Phys. Rev. B*, 2019, **100**, 035406.
- 24 M. Ormazá, L. Fernández, M. Ilyn, A. Magaña, B. Xu, M. J. Verstraete, M. Gastaldo, M. A. Valbuena, P. Gargiani, A. Mugarza, A. Ayuela, L. Vitali, M. Blanco-Rey, F. Schiller and J. E. Ortega, *Nano Lett.*, 2016, **16**, 4230–4235.
- 25 K. Kim, J. Seo, E. Lee, K.-T. Ko, B. S. Kim, B. G. Jang, J. M. Ok, J. Lee, Y. J. Jo, W. Kang, J. H. Shim, C. Kim, H. W. Yeom, B. I. Min, B.-J. Yang and J. S. Kim, *Nat. Mater.*, 2018, **17**, 794–799.
- 26 C. Gong and X. Zhang, *Science*, 2019, **363**, 706.
- 27 L. Smejkal, R. González-Hernández, T. Jungwirth and J. Sinova, *Sci. Adv.*, 2020, **6**, eaaz8809.
- 28 P. Tang, Q. Zhou, G. Xu and S.-C. Zhang, *Nat. Phys.*, 2016, **12**, 1100–1104.
- 29 G. Hua, S. Nie, Z. Song, R. Yu, G. Xu and K. Yao, *Phys. Rev. B*, 2018, **98**, 201116.
- 30 F. Máca, J. Mašek, O. Stelmakhovych, X. Martí, H. Reichlová, K. Uhlířová, P. Beran, P. Wadley, V. Novák and T. Jungwirth, *J. Magn. Magn. Mater.*, 2012, **324**, 1606–1612.
- 31 Q. Lv, P.-H. Fu, Q. Zhuang, X.-L. Yu and J. Wu, *J. Phys.: Condens. Matter*, 2022, **34**, 505702.
- 32 Z. Gao, F. Ma, Z. Zhu, Q. Zhang, Y. Liu, Y. Jiao and A. Du, *Nano Lett.*, 2024, **24**, 10964–10971.
- 33 H. Fernandez, R. Gonzalez-Hernandez, J. Paez, D. M. Hoat, N. Tan Tan, J. Guerrero-Sanchez and E. G. Perez-Tijerina, *J. Phys.: Condens. Matter*, 2024, **36**, 155801.
- 34 G. Kresse and J. Furthmuller, *Comput. Mater. Sci.*, 2019, **6**, 15–50.
- 35 G. Kresse and J. Hafner, *Phys. Rev. B: Condens. Matter Mater. Phys.*, 1993, **48**, 13115.
- 36 J. P. Perdew, K. Burke and M. Ernzerhof, *Phys. Rev. Lett.*, 1996, **77**, 3865.
- 37 J. P. Perdew and Y. Wang, *Phys. Rev. B: Condens. Matter Mater. Phys.*, 1992, **45**, 13244–13249.
- 38 P. E. Blöchl, *Phys. Rev. B: Condens. Matter Mater. Phys.*, 1994, **50**, 17953–17979.
- 39 C. Liu, B. T. Fu, H. B. Yin, G. B. Zhang and C. Dong, *Appl. Phys. Lett.*, 2000, **117**, 103101.
- 40 S. L. Dudarev, G. A. Botton, S. Y. Savrasov, C. J. Humphreys and A. P. Sutton, *Phys. Rev. B*, 1998, **57**, 1505–1509.
- 41 S. Baroni, S. de Gironcoli, A. Dal Corso and P. Giannozzi, *Rev. Mod. Phys.*, 2001, **73**, 515.
- 42 S. Subkow and M. Fähnle, *Phys. Rev. B*, 2009, **80**, 212404.
- 43 N. Rezaei, M. Alaei and H. Akbarzadeh, *Comput. Mater. Sci.*, 2022, **202**, 110947.
- 44 D. Hobbs, G. Kresse and J. Hafner, *Phys. Rev. B*, 2000, **62**, 11556.
- 45 Z. Guo, J. Zhou and Z. Sun, *J. Mater. Chem. A*, 2017, **5**, 23530–23535.
- 46 B. Zhang, J. Zhou and Z. Sun, *J. Mater. Chem. A*, 2022, **10**, 15865–15880.